In Situ Characterization of Floc Morphology by Image Analysis in a Turbulent Taylor–Couette Reactor

Mélody Vlieghe
Université de Toulouse; INPT, UPS; LGC, 4, Allée Emile Monso, F-31030 Toulouse, France

CNRS; Laboratoire de Génie Chimique; F-31030 Toulouse, France

Université de Toulouse; INSA, UPS, INP; LISBP, 135 Avenue de Rangueil, F-31077 Toulouse, France

INRA, UMR792 Ingénierie des Systèmes Biologiques et des Procédés, F-31400 Toulouse, France

CNRS, UMR5504, F-31400 Toulouse, France

Carole Coufort-Saudejaud and Christine Frances
Université de Toulouse; INPT, UPS; LGC, 4, Allée Emile Monso, F-31030 Toulouse, France

CNRS; Laboratoire de Génie Chimique; F-31030 Toulouse, France

Alain Liné
Université de Toulouse; INSA, UPS, INP; LISBP, 135 Avenue de Rangueil, F-31077 Toulouse, France

INRA, UMR792 Ingénierie des Systèmes Biologiques et des Procédés, F-31400 Toulouse, France

CNRS, UMR5504, F-31400 Toulouse, France

DOI 10.1002/aic.14431
Published online March 14, 2014 in Wiley Online Library (wileyonlinelibrary.com)

Flocculation of bentonite was performed in a turbulent Taylor–Couette reactor under various shear rates. Image processing enabled to determine various morphological characteristics of individual flocs. Not only their mean values but also their distributions were studied under various hydrodynamic conditions. Relevant properties were selected. The temporal evolution of radius of gyration and circularity distributions was monitored during the flocculation process. Although size and shape are obviously correlated, this article points out that their dependency to hydrodynamics is different, showing that flocs of similar sizes produced under different hydrodynamic conditions exhibit different shapes. The sizes are calibrated by the turbulence as the double radius of gyration is close to Kolmogorov microscale, whereas the circularity seems correlated to the rotation speed. © 2014 American Institute of Chemical Engineers *AIChE J*, 60: 2389–2403, 2014

Keywords: flocculation, aggregate morphology, image analysis, hydrodynamics

Introduction

The removal of fine particles such as clay from a fluid is an essential part of water treatment. To that end, flocculation processes are used to promote the aggregation of small particles to form flocs that can be more easily removed. The neutralization of surface charges is achieved through the addition of a coagulant and mixing the suspension is required to ensure that the particles encounter one another. The influence of the average shear rate on mean floc size has been widely investigated[1–4] and it is shown that higher shear rates may lead to smaller flocs. Besides, the flow in a mixing tank is highly heterogeneous so the aggregates are subjected to fluctuating stresses during the process that influence significantly the aggregate size distribution.[5–8] Eventually the floc population at the end of a flocculation process is a result of aggregation and breakup events from which the aggregates may undergo structural changes.[9]

The cohesion of flocs, closely related to their structure, affects their ability to settle down, which is important to ensure a correct separation after the flocculation step, usually performed by sedimentation or filtration. Floc interactions with hydrodynamics are highly affected by porosity,[10–12] therefore, aggregation kinetics is influenced by aggregate structure in terms of collision frequency and efficiency,[13,14] as well as aggregate breakup.[15] Structural changes were shown to occur in flocculation experiments where a first quick growth of floc size was followed by a slow and sometimes subtle decrease to finally reach a steady state (SS).[16–18] It can be explained by the fact that when flocs become large enough they get subjected to restructuring or breakup, the resulting fragments can aggregate to form denser, thus

Correspondence concerning this article should be addressed to A. Liné at alain.line@insa-toulouse.fr.

smaller flocs. This explanation is confirmed by breakup and regrowth experiments.[19] However, floc structure observation and quantification is not trivial.

The work of Spicer et al.[16] was one of the first studies that analyzed the change of aggregate size and also morphology (as a perimeter-based fractal dimension) during the flocculation of polystyrene particles. They observed a strong dependency of the size and of the fractal dimension to the average shear rate. They found that the porosity first increased during a phase of floc growth, and then decreased as the breakup occurred and the mean size was stabilized. Li et al.[20] performed flocculation experiments of kaolin with aluminum sulfate under various shear rates in a jar test. They found a very strong correlation between floc characteristics in terms of size, two-dimensional (2-D) fractal dimension, and floc strength (smaller flocs were stronger and denser), all being influenced by the shear rate (the higher the shear rate, the smaller, stronger, and denser the aggregates).

As mentioned above, the floc structure or shape is usually characterized by a fractal dimension. Several definitions for the fractal dimension are found in the literature. They generally take the form of a power law equation $Y \propto X^D$, where X is a length scale (characteristic radius or perimeter), Y is a higher order dimension (area or volume, equivalently mass or number of primary particles), and D is the fractal dimension or a simple function of the fractal dimension. Under certain conditions, an average mass fractal dimension can be identified from the scattering exponent obtained from light scattering analysis.[21] This experimental method is intrusive because of sampling, although it can be performed online with a recycling loop[22–24] with a risk of flow perturbations and thus floc modifications.[19] Another approach to floc characterization is image analysis. Many studies used ex situ destructive methods such as transmission electron microscopy,[25] confocal laser scanning microscopy,[23,24,26,27] or sample analyses coupling a microscope and a CCD camera.[1,20,28–30] Sometimes an advanced sample preparation is implemented to handle fragile flocs. However, to avoid any risk of aggregate alteration due to sample manipulation or flow modification, in situ measurement methods based on advanced imaging techniques were developed.[31–34] In the past decades, some studies used laser sheet lighting.[35–39] An important feature of these systems is the possibility to acquire a large number of images, besides the images have very few out-of-focus objects that are easily removed during image binarization.

Again, among these studies, those working on aggregate morphology measured average fractal dimensions obtained by correlating aggregate projected area to perimeter (perimeter-based fractal dimension) or characteristic length (2-D fractal dimension). As a matter of fact a large majority of flocculation experiments are restricted to average fractal dimension characterization, failing to represent the morphological diversity within a floc population. Measuring individual morphological properties would make it possible to calculate distributions to better observe and comprehend the mutual influences of aggregate size, aggregate shape, and the surrounding hydrodynamics, and to further describe their evolution through population balance modeling.

Some authors studied individual aspect ratios of latex aggregates under various turbulent conditions[23,40] and found that aspect ratio distributions were hardly influenced by the amount of shear or the difference of flow heterogeneities produced by a Taylor–Couette device and a stirred tank. In the past, Gorczyca et al.[41] measured distributions of a shape factor of various mineral flocs. They obtained different distributions, well fitted by log-normal laws with large standard deviations. Recently, morphological image analyses have been run in various application fields such as activated sludge,[42] nanomaterial aggregates,[43] or earthworm casts.[44] These authors studied a large panel of morphological properties of individual objects and classified these properties according to their ability to describe the system and its different characteristic scales.

This work presents experimental data on bentonite flocculation in a Taylor–Couette reactor under controlled turbulent hydrodynamic conditions. To create large and fragile flocs that can be influenced by hydrodynamic stresses, coagulation by charge neutralization was promoted. To generate hydrodynamic stresses that can interact with flocs, varying operating conditions were chosen in a turbulent regime. The distributions of both size and shape parameters describing floc structure over time is of great importance since post-treatment separation efficiency strongly depends on aggregate size and shape. In the present work, an in situ nonintrusive method was developed to determine floc characteristics under various shear rates. High resolution images of flocs were acquired with a CCD camera in a plane illumated by a laser sheet. Images were analyzed to compute accurate size and shape properties of individual aggregates and their distributions. Average values as well as higher order moments can be derived from these distributions. The flocculation system was monitored during the process until a SS was reached. This work provides an experimental database for understanding and modeling aggregation and breakage phenomena under turbulent conditions. The objectives of the present article are to give a nonexhaustive overview of the variety of morphological floc characteristics that can be obtained by image analysis, to select relevant properties describing the morphological diversity of the floc population involved in this study, and eventually to analyze this diversity with respect to varying hydrodynamic conditions.

Experimental Setup

Materials and device

Bentonite from CECA Chemicals was used for the experiments. The properties of this particular type of clay were well described by Luckham and Rossi.[45] The dry primary particles measured by laser diffraction granulometry (MasterSizer2000, Malvern Instruments) have a volume mean diameter of 5 μm. Due to its swelling properties, a 200-mL suspension containing the appropriate quantity to reach the desired mass concentration in the reactor (30 mg L^{-1}) was prepared several days before the experiment.

Aluminum sulfate, which is commonly used in water treatment was chosen as a coagulant. To avoid uncertainties due to small quantity measurements, a large volume of solution was prepared in advance, at a concentration determined to obtain a concentration after dilution equal to 3.5×10^{-5} mol L^{-1}. For each experiment, 5 mL of this solution were sampled with a volumetric pipette, ensuring a constant quality over the experiments. The pH of the suspension after the addition of aluminum sulfate was equal to 4.5 ± 0.1. Considering the equilibrium constant[46] $pK_{Al^{3+}/Al(OH)^{2+}} = 4.95$, the dominant form of aluminum at this pH value is Al^{3+}, which is favorable for coagulation by charge neutralization.

All the experiments were carried out with demineralized water stored in a large (50-L) tank to keep a constant quality

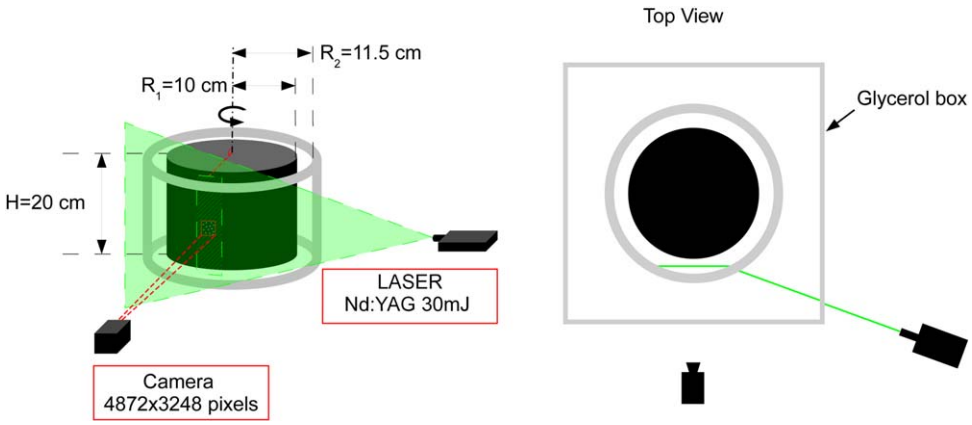

Figure 1. Experimental setup.

[Color figure can be viewed in the online issue, which is available at wileyonlinelibrary.com.]

and to avoid bubble formation during the experiments. Experiments were done at room temperature, ranging between 20 and 25°C.

The experiments were performed within a Taylor–Couette apparatus (see Figure 1) composed of an inner cylinder of 10 cm in radius (R_1) made of black PVC and an outer cylinder of 11.5 cm in radius (R_2) made of transparent plexiglas. The height of the cylinders is $H = 20$ cm and the reactor volume is 2 L. The outer cylinder is fixed while the inner one rotates at an adjustable speed N. Hydrodynamics in this reactor were characterized in a previous work[6] by particle image velocimetry (PIV) measurements and computational fluid dynamics (CFD) simulations. The hydrodynamic regime in the Taylor–Couette reactor is characterized by the Taylor number defined as

$$Ta = \frac{\Omega^2 R_1 (R_2 - R_1)^3}{\upsilon^2} \quad (1)$$

where Ω (s^{-1}) is the angular velocity of the inner cylinder and υ ($m^2\ s^{-1}$) is the kinematic viscosity of the fluid.

Experimental protocol

Before starting an experiment, the primary suspension was vigorously agitated with a magnetic stirrer during 45 min to break any aggregate formed during the swelling period. Water was poured into the Taylor–Couette vessel and the rotation speed was set to 100 rpm before adding the bentonite suspension. The quick addition of aluminum sulfate was immediately followed by a 3-min phase of aggregation at a high rotation speed (100 rpm). The global shear rate was then equal to 325 s^{-1}. This short period, assimilated to a coagulation phase, participated to create identical initial conditions before the rotation speed of the inner cylinder was set to the desired value. Aggregation was then carried out at 30, 50, 70, or 90 rpm providing global average shear rate values of 75, 130, 190 or 280 s^{-1}, respectively, and Taylor number values of $3.3\times10^6, 9.3\times10^6, 1.8\times10^7$, and 3.0×10^7, respectively. The observed hydrodynamic regime corresponds to turbulent Taylor vortex flow.

Image acquisition

Aggregation was monitored by taking floc pictures. A laser sheet (Nd:Yag 532 nm, 30 mJ) was used to illuminate a tangential plane in the gap between the cylinders as shown on Figure 1. A CCD camera (FlowSense EO 16M, 4872×3248 pixels^2), synchronized with the laser sheet, acquired grayscale floc pictures with a spatial resolution of 7.3 μm/pixel. Pictures were taken at a frequency of 4 Hz (low enough to avoid any risk of accounting for the same aggregate on two consecutive pictures). Each acquisition consisted of taking 70 pictures, so the instantaneous results were averaged over 18 s. The time value of a measurement was recorded as the first image was acquired. The acquisition frequency was then limited by the recording time after each acquisition. Thus, the shortest possible time between each measurement was about 2 min. To reduce the amount of data stored this time was extended as the flocculation proceeded.

To quantify floc size and morphology, the image quality is of high importance. Thus, the refraction through the outer cylinder walls was an issue that needed to be treated with care. For this purpose, the Taylor–Couette apparatus was enclosed within a cubical box made of Plexiglas (as is the outer cylinder) and filled with glycerol. Indeed, the refractive index of glycerol (1.47) is close to the refractive index of Plexiglas (1.51), considerably reducing the refraction effect. Besides, the camera was placed so that the optical axis was as perpendicular as feasible to all the interfaces, and positioned so that the length of the image (39 mm) was vertical and the width (26 mm) was horizontal, to minimize the angles of the curved interface.

Image Analysis Protocol

Image treatment

To detect and isolate the image regions where the flocs appear, image binarization was performed by applying a gray level threshold. The efforts made to obtain high quality images aimed in particular at reducing as much as possible the need for image treatment. As an example, a 270×180 pixels^2 portion of a raw image is shown on Figure 2a. However, applying a threshold on raw images would produce artificial holes and surface irregularities on the aggregates (see Figure 2b) because the intrinsic heterogeneity of bentonite resulted in a great irregularity of gray levels on the floc images. Thus a circular averaging filter of 1 pixel radius was applied to the raw images (Figure 2a) to slightly smooth these fake irregularities. The effect of this smoothing is shown on Figure 2c. The gray level threshold was then

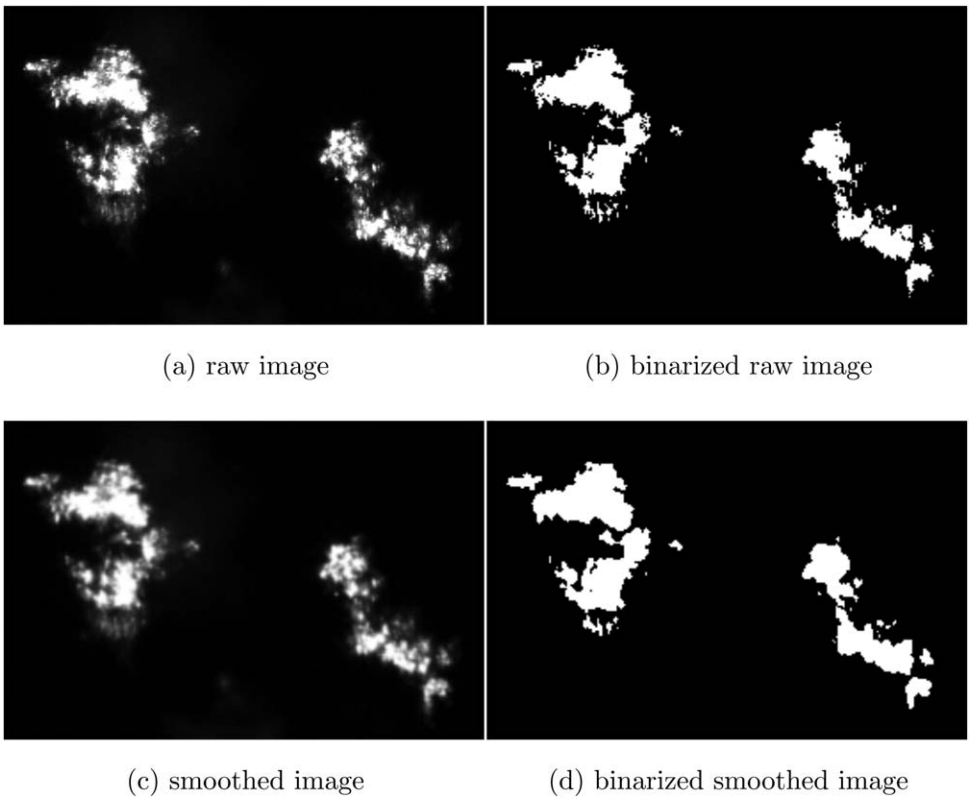

Figure 2. Image processing.

determined by applying Otsu's method[47] on each image with the Matlab function *graythresh*. The principle of this method is to maximize the separability of the classes by optimizing the between-class variance. The resulting binarized image is shown on Figure 2d.

Particle image analysis

Binarized images were analyzed using a Matlab function named *regionprops*. The outputs directly computed by *regionprops* are listed in Table 1. However, the estimation of the perimeter has been improved and other characteristic properties have been introduced.

Perimeter. The perimeter value provided by *regionprops* function measures the cumulated distance between the centers of the pixels belonging to the region and lying on its boundary. This calculation underestimates the aggregate perimeter. It is accurate enough if the region is composed of a great number of pixels, but it can be an issue if aggregates are composed of only a few dozens of pixels. As an example, the perimeter of a square made of 10×10 pixels^2 will be estimated as 36 pixels instead of 40, that is, a 10% error. To compensate for this drawback, another estimated perimeter was calculated by building an enlarged region composed by the initial region plus the surrounding pixels, and computing an overestimated perimeter by applying the function *regionprops* to the enlarged region. Eventually, the perimeter P was estimated as the average of the underestimated and overestimated perimeters.

Radius of gyration. The radius of gyration R_g is a characteristic length scale of the (projected) particle that takes into account pixel positions with respect to the centroid. In mechanics, it is defined as the distance to an axis where all the object mass would be concentrated and rotate with the same mass moment of inertia. It can be obtained from the root mean square of the pixel-to-centroid distances

Table 1. Aggregate Image Properties Directly Computed by *regionprops* (Lengths in Pixel Units are Converted Before Use)

Property	Notation	Definition
Area	A	Cumulated pixel area
Perimeter	P	Cumulated distance between boundary pixels
Circle equivalent diameter	CED	Diameter of the circle of area: CED $=\sqrt{4A/\pi}$
Centroid coordinates	x_c,y_c	Mass center coordinates (average coordinates) $(x_c, y_c)=\frac{1}{A}\sum_i^A (x_i, y_i)$
Convex hull area and perimeter	A_{CH} , P_{CH}	Properties of the smallest convex region that contains the projected particle
Solidity	S	Ratio of the actual area over the convex hull area: $S=A/A_{CH}$
Major and minor axes	L,l	Axes of the second-order moments equivalent ellipse
Aspect ratio	AR	AR $= l/L$

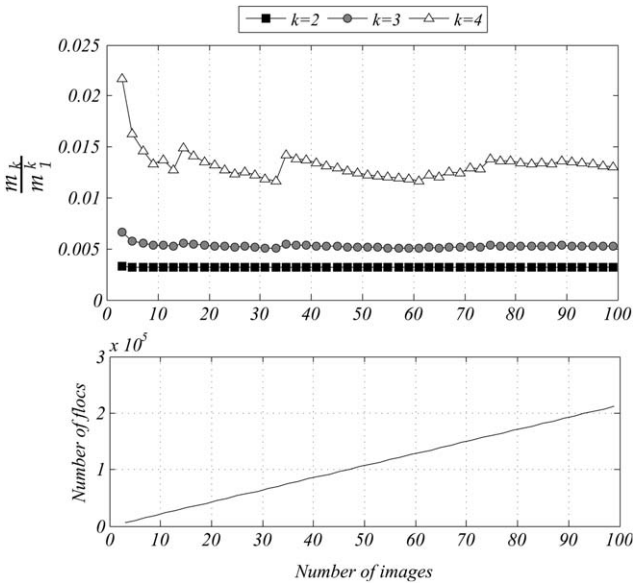

Figure 3. Area distribution normalized moments and number of flocs analyzed vs. the number of images.

$$R_g^2 = \frac{1}{N_p}\sum_{i=1}^{N_p}\left[(x_i - x_c)^2 + (y_i - y_c)^2\right] \quad (2)$$

where N_p denotes the number of pixels on the aggregate, (x_i,y_i) are pixel coordinates, and (x_c,y_c) are centroid coordinates.

Circularity and convexity. To quantify the shape of an aggregate, one can consider several scales and focus on either the overall shape, the presence of concavities, or the surface roughness. Small scale irregularities can have a major impact on the perimeter without significant changes on the area, so parameters involving the aggregate perimeter generally focus more on surface roughness than parameters involving the aggregate area which rather characterize the overall shape. As a complement to the morphological parameters directly provided by Matlab (Table 1), two parameters defined as perimeter ratios were calculated.

The convexity Cv is defined as the ratio of the convex hull perimeter P_{CH} (see Table 1) over the actual perimeter (Eq. 3). As its name suggests, it quantifies how convex the floc image is, that is, it accounts for concavities and boundary roughness (the convexity of a circle as well as of a square is 1). Compared to the solidity defined with area ratio instead of perimeter ratio (see Table 1), the convexity definition focuses more on the surface aspect than on the space distribution of mass

$$\mathrm{Cv} = \frac{P_{CH}}{P} \quad (3)$$

The circularity Ci is defined as the circle equivalent perimeter divided by the actual perimeter (Eq. 4). It describes how close to a circle the aggregate image is, taking into account the overall shape as well as the boundary roughness (the circularity of a circle is 1, the one of a square is 0.886)

$$\mathrm{Ci} = \frac{\sqrt{4\pi A}}{P} \quad (4)$$

Values of circularity and convexity range between 0 and 1. In practice, values up to 1.1 are obtained for small aggregates because of the lack of accuracy of the perimeter estimation. Without the improvement explained above, values greater than 2 would be obtained.

Image analysis validation

The aim of this work was to provide an experimental database for understanding and modeling aggregation and breakage phenomena under turbulent conditions. It was necessary to acquire a high enough number of flocs (hence of images) to provide accurate data, not only in terms of mean values but also in terms of higher order moments of the measured distributions. The k^{th} order moment of the distribution $n(X)$ is defined and computed as in Eq. 5. The aggregates are first distributed in classes according to the property X taking a finite number of values X_i. Y_i is the amount (surface fraction,

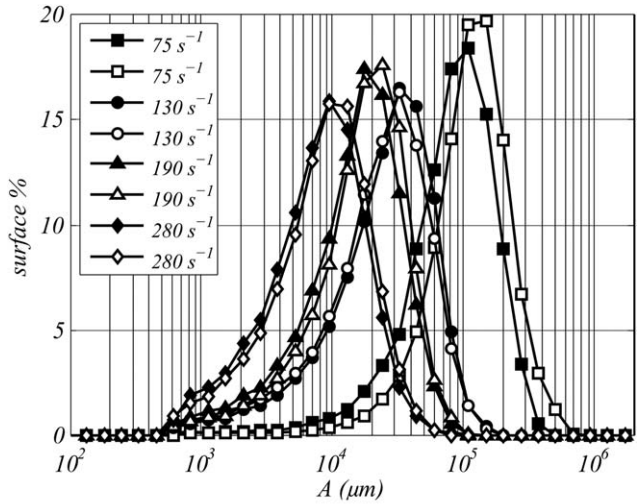

(a) Area

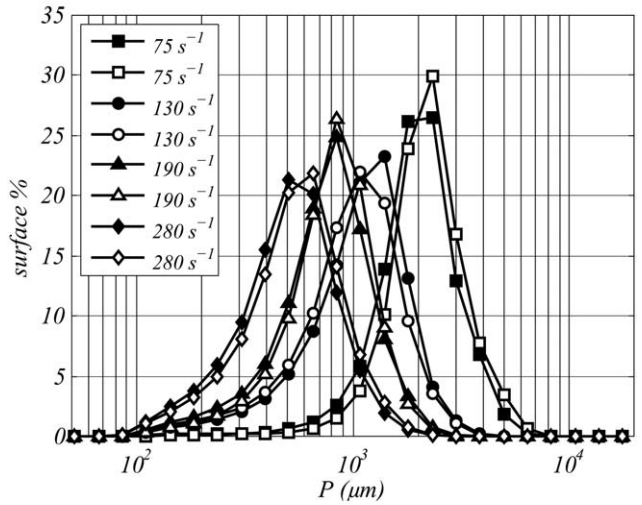

(b) Perimeter

Figure 4. Steady state (SS) surface distributions of aggregate area obtained for eight experiments at fourfour different shear rates.

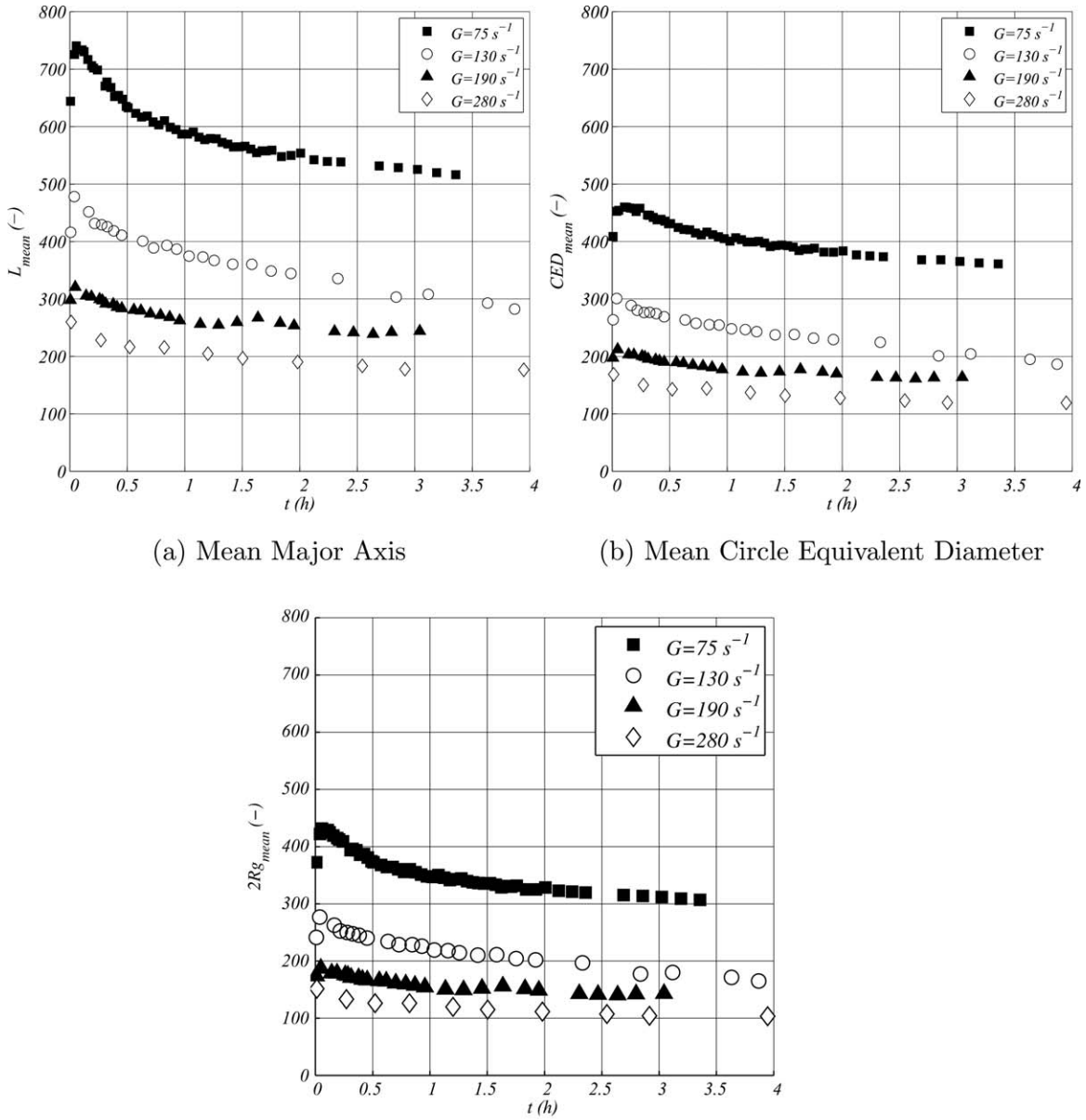

Figure 5. Mean values of size properties vs. time.

in the case of a surface distribution) of aggregates belonging to the class $[X_i, X_{i+1}]$

$$m_k = \int_0^\infty (X) X^k dX = n \sum_i \int_{X_i}^{X_{i+1}} n(X) X^k dX \approx \sum_i \frac{Y_i \left(X_{i+1}^{k+1} - X_i^{k+1} \right)}{(k+1)(X_{i+1} - X_i)} \tag{5}$$

Moreover, the acquisition frequency of 4 Hz limited the time resolution. A compromise was made considering 70 images per acquisition, implying an acquisition time of 18 s, meaning that the measured properties are averaged over 18 s, which is small compared to the time scale of the flocculation process (3–4 h). Figure 3 shows the moments of the surface distributions of floc area vs. the number of analyzed images, as well as the corresponding number of flocs. For the sake of readability, the moments are normalized as m_k/m_1^k. With 70 images, that is, 1.5×10^5 flocs, the convergence is satisfactory. Note that better convergence results are obtained on area distributions at lower shear rates, as well as on perimeter distributions, and on area and perimeter number distributions.

To verify the experimental repeatability, the same experiment was carried out twice at each rotation speed. The area and perimeter distributions obtained at SS are shown, respectively, on Figures 4a and 4b, since these two parameters are the main basic data from which other relevant properties are derived. The repeatability is good although not perfect, especially concerning the area distribution at the lowest shear rate. According to [19], the experimental protocol consisting in injecting the coagulant after the suspension setting up could lead to reproducibility issues. Besides, the setting up of the initial condition is a delicate and determining step,

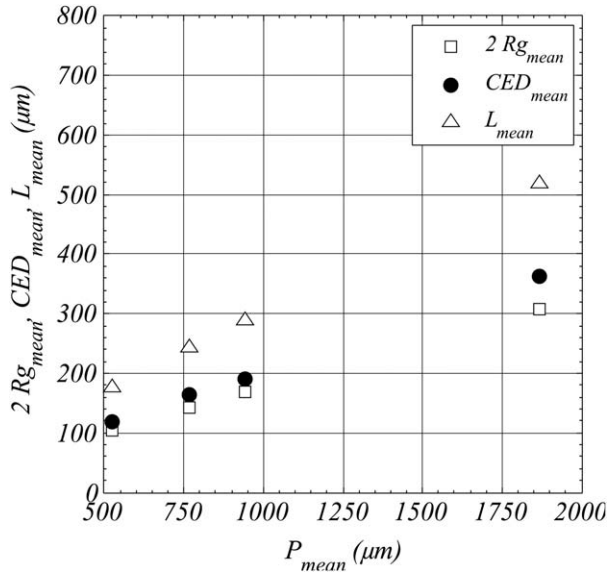

Figure 6. Comparison of the SS mean values of size properties obtained under different turbulent conditions.

which is confirmed by the fact that the slight gap between the two distributions obtained at 75 s^{-1} appeared from the first measurements (so it can be attributed to initial condition fluctuations). However, the similarity of the distributions shown on Figure 4 is fully satisfactory, as are the time evolutions.

Results and Discussion

The results are presented as surface distributions rather than number distributions which attach a relative importance to the smallest aggregates, which constitute a small amount of the overall mass and are less accurately characterized by our imaging system. To ensure a relevant morphological characterization, only aggregate images composed of 10 pixels or more were taken into account, thus the smallest aggregates analyzed have a CED of 26 μm, the minimum R_g and L detected are, respectively, 9 and 28 μm. These aggregates are composed of very few primary particles and will be named primary aggregates.

Change of the mean floc characteristics

As suggested by Figure 4, the surface distributions of the floc properties remain monomodal all along the experiments. Therefore, the time evolution of the mean values of the floc characteristics was first considered. The time reference is the change from 100 rpm to the desired rotation speed. One can distinguish between properties characterizing either size or shape.

Size properties. The changes of the mean values of the circle equivalent diameter CED, the radius of gyration R_g, and the major axis length L vs. time are reported on Figure 5. To be compared with the other two lengths, twice the radius of gyration is reported (see Figure 5c).

These characteristic length scales tend to higher values when the shear rate is lower. Moreover, they evolve in very similar ways. Whatever the shear rate, the sizes tend to grow during the first minutes and then slowly decrease in time because of breakage and restructuring. After 3–4 h, a SS is reached for all the experiments. At the highest shear rate, one cannot distinguish a growth phase but only a decrease. The extent of the restructuring phenomenon can be compared by dividing the maximum size measured, defining the point of maximum growth (MG) referred to below, by the size reached at the SS (similarly to what was done by François[15] concerning floc strength and breakage experiments). The maximum size measured is thus an estimation of the maximum size reached. The ratio of the SS size over the maximum size (either CED, R_g, or L) is about 70% and does not depend on the average shear rate.

These three length scales evolve very similarly. Another view of the results is proposed on Figure 6, where the mean length scales at SS are plotted vs. the corresponding mean perimeters. The various length scales P, CED, L, and R_g are obviously related to each other, suggesting that studying only one of them would provide sufficient information about the size evolution. The choice of a relevant size property will be presented below. If the projected images of the aggregates were disks, the following two equations would be verified: $\mathrm{CED} = L$ and $2R_g = \mathrm{CED}/\sqrt{2}$. Here L_{mean} is generally much higher than CED_{mean}, and $2R_{gmean}$ is very close to CED_{mean}. This is a first evidence that the shapes are not circular, thus the aggregates are not spherical. The analysis of shape properties is thus relevant.

Shape properties. As mentioned in the introduction of this article, the floc shape is often characterized by a fractal dimension. The information provided by the image analysis allows calculating a 2-D fractal dimension Df defined by the relation $A \propto L^{Df}$. This 2-D fractal dimension would be equal to 2 in the case of a circle. Df is obtained by performing a linear regression on the scatter graph obtained by plotting $\log(A)$ vs. $\log(L)$. The result is an average fractal dimension that characterizes the entire floc population and that can be computed at each time. Note that, contrary to the shape properties defined above, which were measured on flocs composed of more than 10 pixels, Df was determined on a scatter graph containing the data for all the flocs. Indeed, applying a filter on the size would come down to cutting out a part of the scatter graph following a straight line, thus biasing the result of the linear regression. The values obtained were all close to $\mathrm{Df} = 1.8$ and did not vary with time nor with the hydrodynamic conditions. Therefore, the information provided by this result remains global and seems to be weakly discriminant.

The change of the mean values of the shape properties aspect ratio AR, solidity S, convexity Cv, and circularity Ci vs. time are shown on Figure 7. The aspect ratio (7a) and the solidity (7b) do not seem to be correlated with the shear conditions. The values of AR_{mean} and S_{mean} increase at the beginning of the experiments, especially at the lower shear rate and become constant after 1 h, while the sizes are still increasing. The values of AR_{mean} are all about 0.65. As previously observed by Ehrl et al.,[40] the global shape is not much affected by hydrodynamics and the aspect ratio is probably not relevant enough to discriminate between different morphologies. One can notice that an ellipse having a ratio of minor axis length over major axis length equal to 0.65 would verify $2R_g = 0.6L$, which is consistent with the values of R_{gmean} and L_{mean} obtained (Figures 5c and 5a). The values of S_{mean} lie between 0.8 and 0.85. The convex area and the actual area are close, indicating the absence of large concavities. AR and S both characterize floc shape at large scales. They both increase only at the early stage of floc growth. A possible explanation is that the first flocs, composed of very few primary aggregates, are more likely to present elongated or curved shapes with relatively low AR

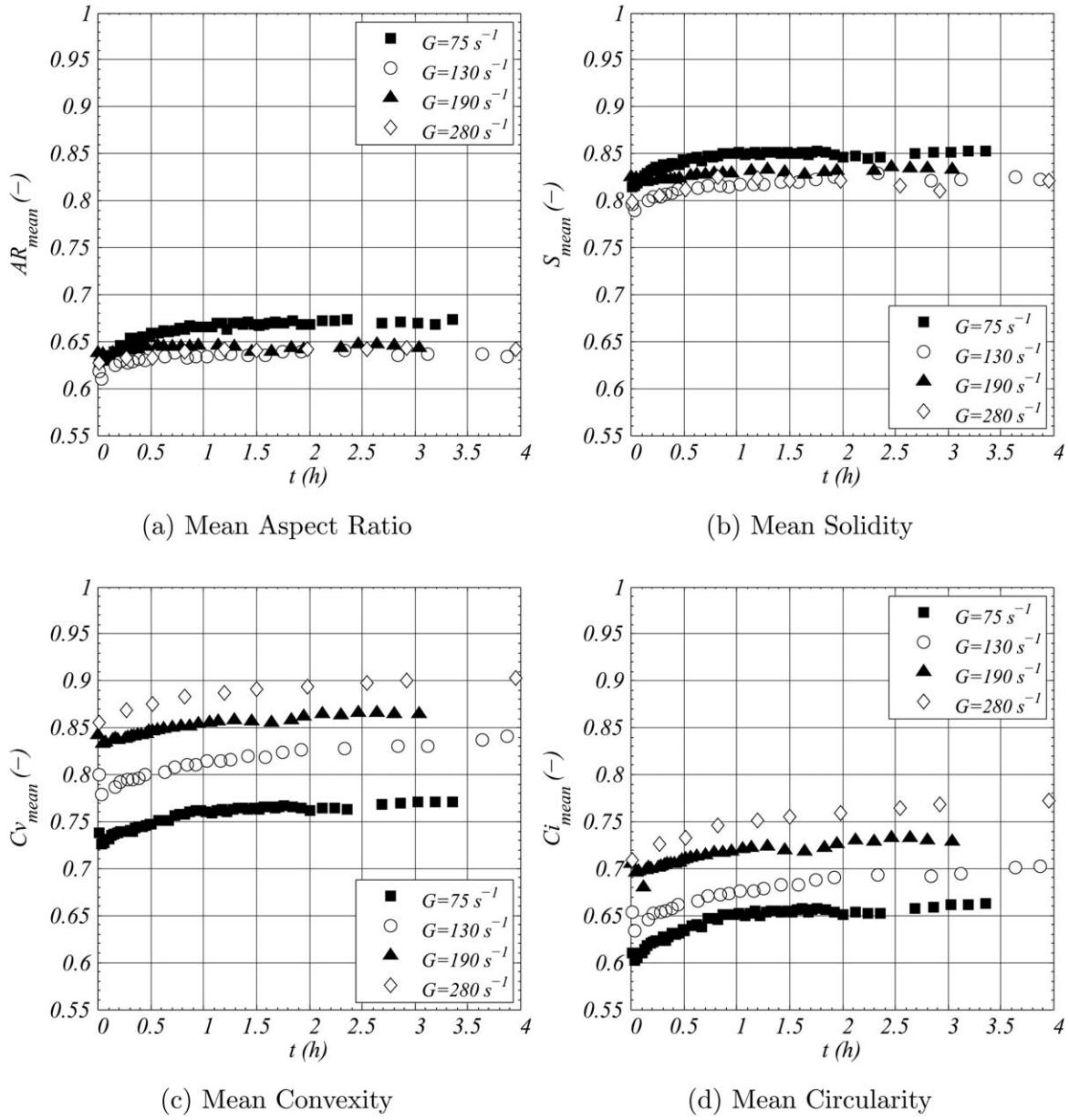

Figure 7. Mean values of shape properties vs. time.

and *S*. After a short time, flocs are composed of higher numbers of primary aggregates that allow less elongated shapes to be formed and large concavities to disappear.

On the opposite, the convexity (7c) and the circularity (7d) evolve as long as the sizes do. First a decrease occurs, in a period concomitant with the growth phase observed on Figure 5. Then Cv_{mean} and Ci_{mean} increase and eventually stabilize. Their evolution is in concordance with the size evolution, confirming the change of floc structure during the flocculation. First, the growth phase produces coarse flocs with irregular shapes, then the restructuring occurs and the shapes become smoother and rounder. At any time, Cv_{mean} and Ci_{mean} values are lower at lower shear rates, indicating a strong correlation of the floc shape with hydrodynamics. However, since the floc sizes are also strongly depending on hydrodynamics, the question of size-independent effects of hydrodynamics on the floc shape is still open at this point.

On Figure 8, the mean shape properties at SS are plotted vs. $\sqrt{4\pi A_{\text{mean}}}/P_{\text{mean}}$. As expected from the previous observations, the aspect ratio and the solidity do not vary significantly. On the contrary, it is interesting to see that the convexity and the circularity follow exactly the same trend. These properties both characterize floc shape at smaller scales (in comparison with AR and *S*). The convexity compares the convex perimeter to the actual perimeter of the projected floc image, so it characterizes the roughness of the floc surface. The circularity compares the circle equivalent perimeter to the actual perimeter so it characterizes both the overall shape and the surface roughness. Given that the overall shape (AR) has been shown not to change significantly, in this case Cv and Ci account for similar shape characteristics. Furthermore, the parameter $\sqrt{4\pi A_{\text{mean}}}/P_{\text{mean}}$ is expressed as a circularity involving mean area and mean perimeter. It can be seen that decreasing the rotation speed, the mean circularity points deviate from the first bisector, indicating that the population of flocs present a larger variety of shapes.

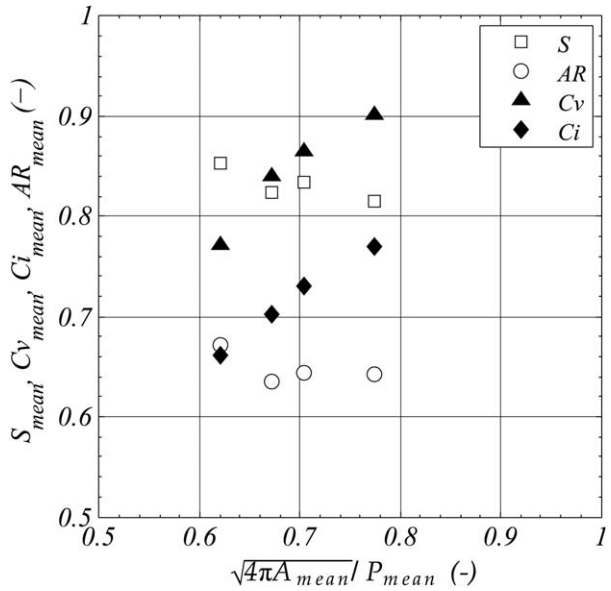

Figure 8. Comparison of the SS mean values of shape properties obtained under different turbulent conditions.

Time evolution of R_g and Ci distributions

To move further on the result analysis, the next part will focus on the floc property distributions. To that end, it is convenient to reduce the number of properties of interest. An overview of the various properties showed that some of them provide redundant information, whereas some properties seem less relevant than others. To properly choose one size variable and one shape variable to monitor, principal component analysis (PCA) was used (see Appendix A). The PCA performed over all aggregate properties confirmed that it is relevant to distinguish between size properties and shape properties. For this reason, PCA was then performed over two groups thus defined. The radius of gyration was selected as a relevant size property and the circularity was selected as a relevant shape property.

On the following, the results are thus discussed on the base of the radius of gyration and circularity, which were shown sufficient to describe the system.

The time evolutions of R_g (resp. Ci) distributions obtained under four different turbulent regimes are plotted on Figure 9 (resp. 10). On each graph, the initial distribution is the one obtained after a period of 3 min during which the rotation speed was equal to 100 rpm and the global shear rate was

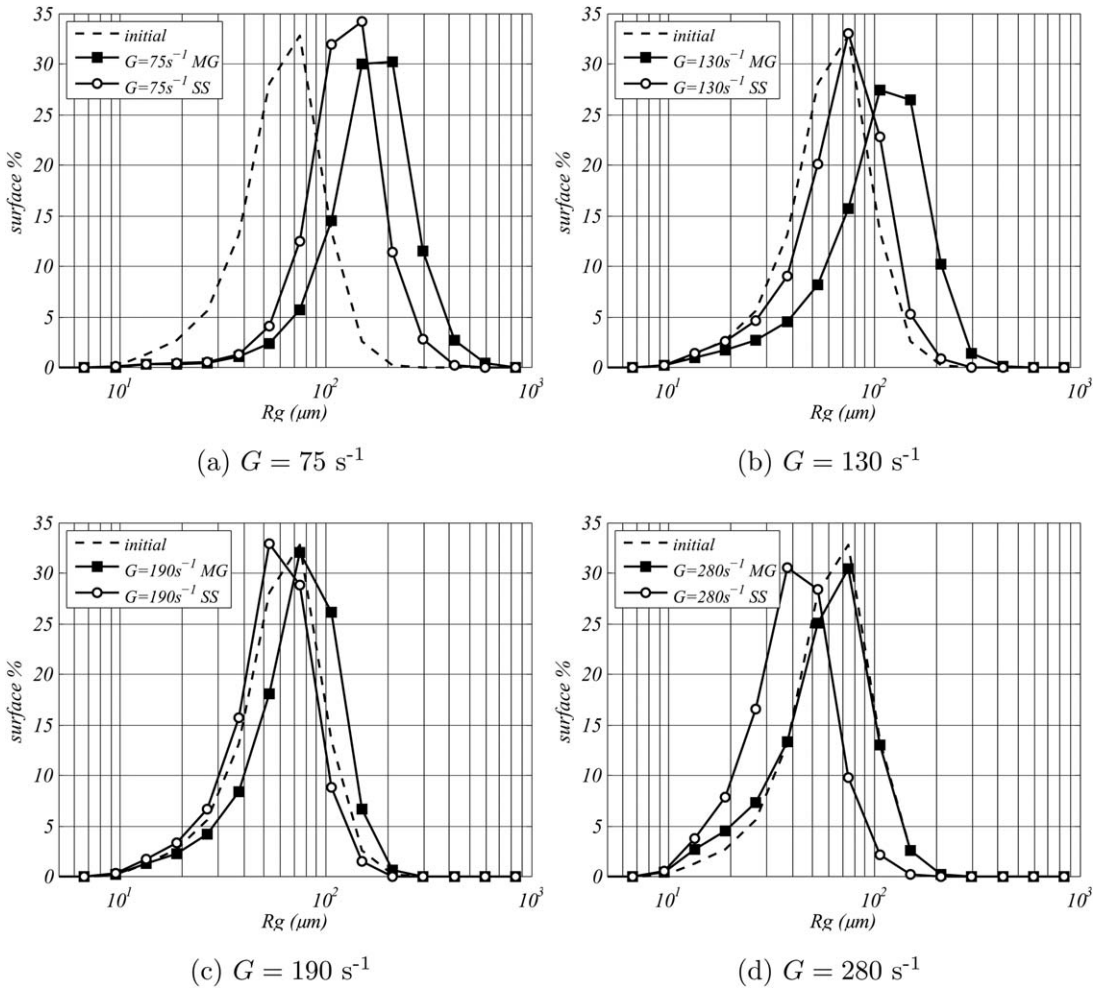

(a) $G = 75$ s^{-1} (b) $G = 130$ s^{-1}

(c) $G = 190$ s^{-1} (d) $G = 280$ s^{-1}

Figure 9. R_g surface distributions over time.

Table 2. R_g and Ci Distribution Characteristics

	R_g				Ci			
	σ (μm)	σ/m_1	S	$\kappa-3$	σ	σ/m_1	s	$\kappa-3$
Initial	35	0.45	+1.0	2.7	0.097	0.13	−0.53	−0.06
G=75s^{-1}MG	103	0.48	+1.2	3.1	0.11	0.18	−0.11	−0.46
G=75s^{-1}SS	68	0.43	+1.1	2.7	0.10	0.16	−0.31	−0.33
G=130s^{-1}MG	71	0.51	+0.9	1.8	0.12	0.19	−0.035	−0.51
G=130s^{-1}SS	42	0.47	+0.9	1.6	0.10	0.15	−0.35	−0.29
G=190s^{-1}MG	43	0.45	+0.7	1.0	0.10	0.15	−0.35	−0.28
G=190s^{-1}SS	32	0.45	+0.9	1.9	0.097	0.13	−0.53	0.00086
G=280s^{-1}MG	37	0.49	+0.9	1.7	0.11	0.15	−0.32	−0.32
G=280s^{-1}SS	25	0.48	+1.5	5.7	0.093	0.12	−0.63	0.11

$G = 325$ s^{-1}. The second distribution corresponds to the point of MG on Figure 5 and the third one is the SS distribution. In Table 2, the characteristics of these distributions in terms of standard deviation (σ and σ/m_1, m_1 being the mean), skewness (s), and excess kurtosis ($\kappa-3$) are presented. The skewness is positive (resp. negative) for a right-tailed (resp. left-tailed) distribution and zero for a symmetrical distribution. The kurtosis κ of a normal distribution being equal to 3, negative values of the excess kurtosis $\kappa-3$ indicate wide peaks and thin tails, compared to those of a normal distribution.

Focusing first on the initial population, the high-shear mixing phase produced a population of aggregates having radius of gyration spread between 10 and 200 μm, the smallest sizes belonging to primary aggregates composed of very few particles. The initial circularity distribution ranges between 0.35 and 0.95, indicating that the initial agglomerates have various nonspherical shapes.

At 75 s^{-1} (30 rpm), the growth phase produced a wide distribution of R_g (Figure 9a). Large flocs are formed and the small sizes that were largely represented on the initial distribution practically disappear, resulting in a positive and

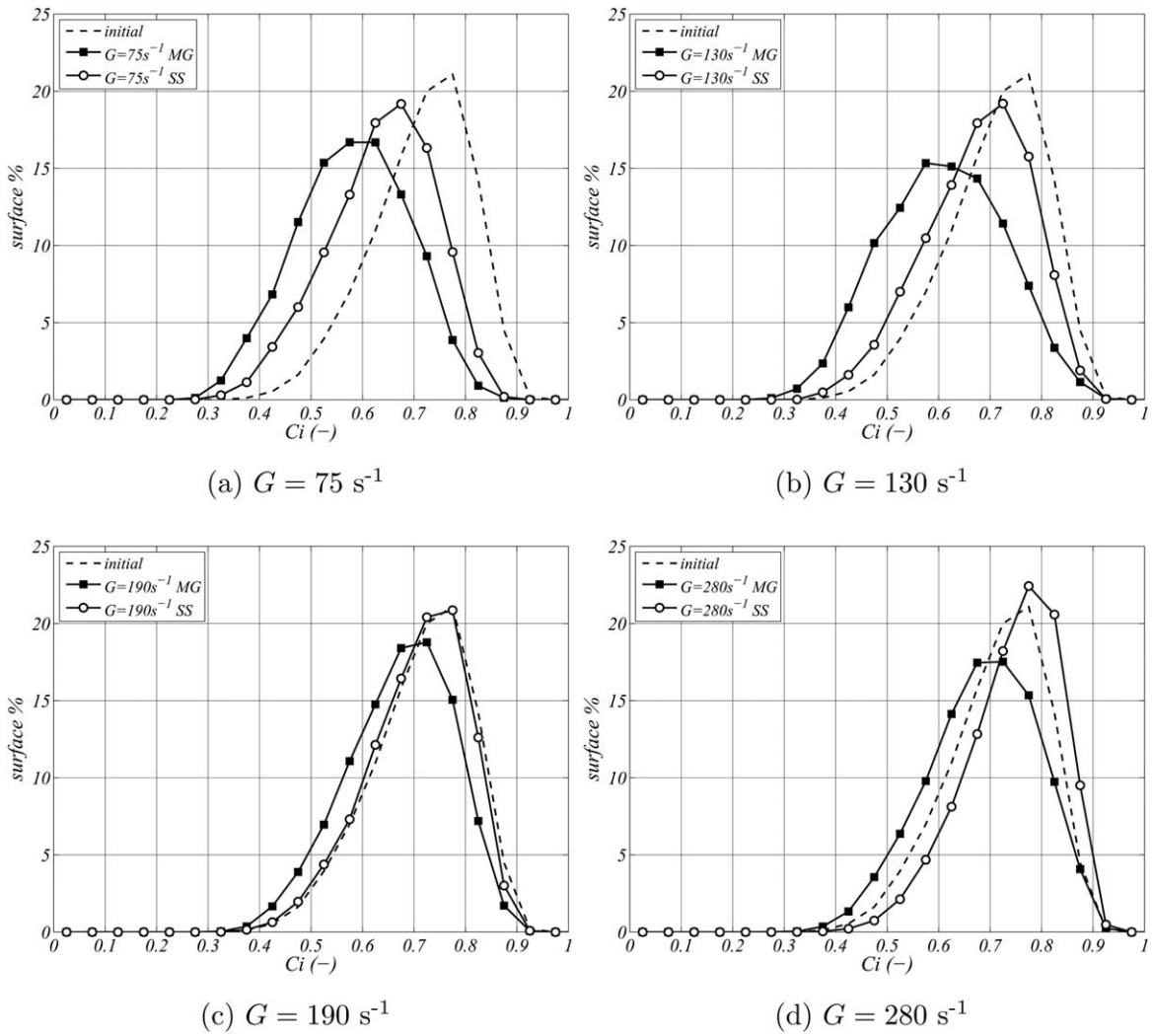

Figure 10. Ci surface distributions over time.

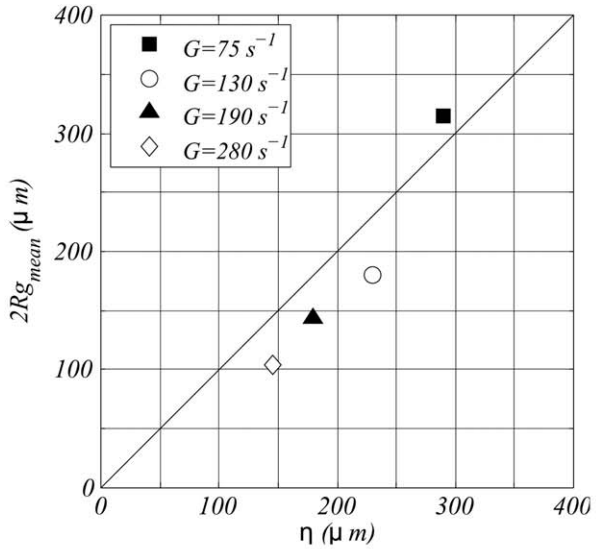

(a) Steady state mean Rg versus Kolmogorov microscale

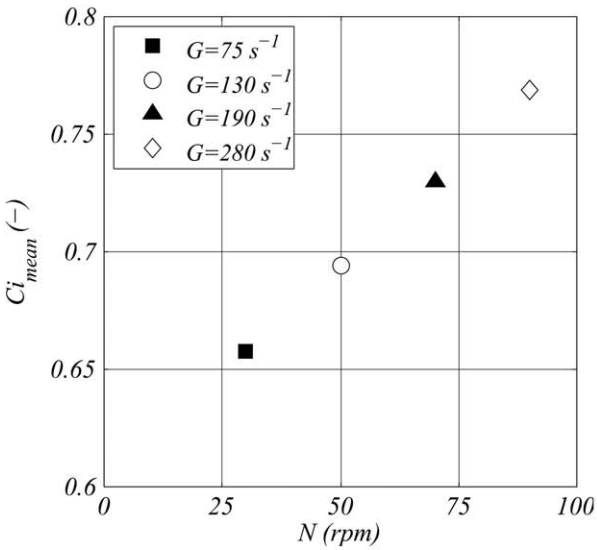

(b) Steady state mean Ci versus rotation speed

Figure 11. SS mean values of R_g and Ci compared to hydrodynamic characteristics.

relatively high value of the skewness. The large excess kurtosis indicates that the peak value is largely represented but so are the extreme values. During a second phase, the R_g distribution slowly translates backward. The largest flocs formed during the growth phase disappear but the small aggregates do not reappear, indicating floc restructuring. The distribution gets sharper with lower standard deviation, skewness, and kurtosis.

At higher shear rates (Figures 9b–d), a clear difference in the evolution of the radius of gyration distribution is noticed. The smallest population of aggregates is always present, either because they do not aggregate, or because of floc breakage. This is characterized by lower values of the positive skewness. Still, a quick growth occurs but it is less significant as the shear rate increases, to the advantage of breakage and restructuring phenomena, to such an extent that the highest shear rate produces a floc population much smaller than the initial one. The absolute values of the standard deviation decrease when the shear rate increases but the normalized values are all comparable (the shapes of the distributions are similar around different mean values), with values slightly decreasing between the growth phase and the SS.

Regarding the circularity distributions (Figure 10), two different distribution shapes are observed after the growth phases at the two lowest shear rates and the two highest. The distributions after the growth phases at 75 and 130 s^{-1} are close to symmetrical (low skewness in Table 2) and exhibit wide peaks and thin tails, as indicated by the large values of negative excess kurtosis in Table 2. At 75 s^{-1}, the growth phase produced a population of less circular flocs, with large circularity values (above 0.85) vanishing, corroborating the assumption that the highest circularity values belong to the smallest aggregates.

At higher shear rates (Figures 10c, d), the circularity distributions after the growth phase are less wide, asymmetric (relatively large negative values of the skewness in Table 2) and the peaks are sharper (lower values of excess kurtosis in Table 2).

During the breakage and restructuring phase, the same trend is observed at all the shear rates. The left tails of the distributions are shifted to the right, that is, the lowest nonempty class becomes empty, while the right tail fills up, that is, the highest nonempty class remains the same and is more represented. This produces asymmetric SS distributions with increased values of negative skewnesses (Table 2).

Whatever the shear rate, the growth phase produces a large variety of floc sizes and shapes (the lower the shear rate, the larger the distribution). The longest phase is constituted by a slow and smooth decrease in size together with an increase in Ci values, indicating restructuring. Only the lower SS allowed to flocculate practically all the smallest aggregates (remind that particles composed of less than 10 pixels are not considered and that the surface distributions naturally attribute less importance to the smallest aggregates) while they remain largely represented at the higher shear rates.

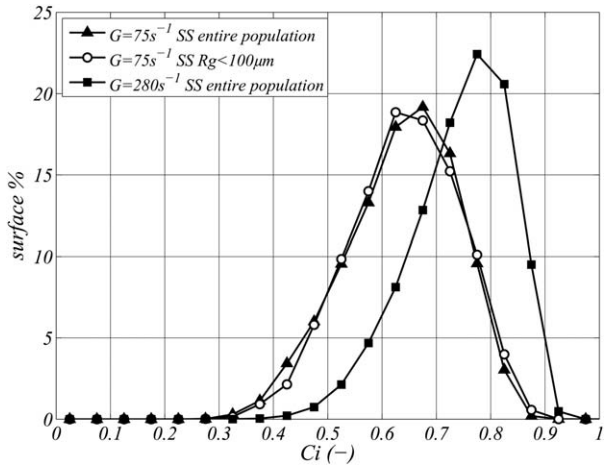

Figure 12. SS Ci surface distribution at $G = 75$ s^{-1}, small flocs compared to the entire population.

Influence of hydrodynamics

To clarify and quantify the influence of hydrodynamics on the radius of gyration and the aggregate circularity, the mean values obtained at the SS were represented on Figure 11. The final mean values of R_g are compared with Kolmogorov microscale η on Figure 11a, whereas the final mean values of Ci are plotted vs. the rotation speed N. The η values used on Figure 11a are modes (which have a more physical sense than mean values) of η distributions.[6] It is clear from Figure 11a that the sizes (especially the largest sizes, since surface distributions are considered) are calibrated by the microscales of turbulence, while the circularity (11b) evolves linearly with the rotation speed of the inner cylinder. Thus, both size and shape are strongly affected by hydrodynamics, but through different flow characteristics.

Furthermore, a fraction of the SS floc population obtained at $G = 75\ s^{-1}$ was selected with the criterion $R_g < 100$ μm. The size distribution of these small flocs formed at 75 s^{-1} is comparable to the one obtained at 280 s^{-1}, so if the circularity was only correlated to the size, the Ci distribution of the small flocs formed at 75 s^{-1} would also be comparable to the one obtained at 280 s^{-1}. Figure 12 compares the circularity distribution of this fraction of small flocs formed at 75 s^{-1} to the ones obtained for the entire population at 75 and 280 s^{-1}. It is clear that the Ci distribution of small flocs formed at 75 s^{-1} is very different from the ones obtained at 280 s^{-1}. Flocs of comparable sizes formed under different shear rates exhibit dissimilar circularity distributions. Moreover, the Ci distribution of small flocs formed at 75 s^{-1} overlaps the ones obtained for the entire population formed at 75 s^{-1}, except for some high values slightly more represented in the case of the small flocs. The morphological diversity observed for the entire population is just as well represented by the smallest flocs. It means that the observed difference in aggregate circularity distributions obtained under different hydrodynamic conditions is not only due to different sizes. Hydrodynamics indeed has a size-independent influence on floc shape.

Conclusions

Bentonite flocculation experiments were performed under four turbulent conditions in a Taylor–Couette reactor to study floc size and morphology. High resolution images were acquired in a plane illuminated by a laser sheet, to precisely characterize the variety of floc sizes and shapes. For each measurement, a large number of images (70) were analyzed to provide converged distributions of floc properties. The flocculation was monitored at the highest feasible frequency (every few minutes) over a long enough period of time (3–4 h) to reach a SS. It was shown that the various size properties are correlated despite the shape diversity. On the opposite, different shape properties characterize different scales of floc morphology and not all of them are discriminant. In this particular system, the overall shape was not relevant to describe the flocs. The circularity was chosen to be studied. This shape property accounts for the overall shape of a floc as well as the roughness of its boundary. During the flocculation, two phases could be detected: a first rapid phase of growth during which the size increases and the circularity decreases (the higher the shear rate, the stronger this trend), and a second slow phase, usually interpreted as breakage and restructuring, during which the size decreases and the circularity increases. The surface distributions of radius of gyration and circularity were analyzed at the end of the growth phase and at the SS. The parallel evolution of the shape of the distributions showed that high values of circularity are due to small flocs and low values of circularity are related to the presence of large flocs. However, the SS mean values of R_g and Ci are not related to the same hydrodynamic characteristics. The sizes are calibrated by the turbulence as double the radius of gyration is close to Kolmogorov microscale, whereas the circularity seems correlated to the rotation speed. This database will be used to develop population balance modeling.

Notation

A = area, μm^2
A_{CH} = convex area, μm^2
AR = aspect ratio, -
CED = circle equivalent diameter, μm
Ci = circularity, -
Cv = convexity, -
Df = two-dimensional fractal dimension, -
G = global shear rate, s^{-1}
L = major axis length, μm
l = minor axis length, μm
m_k = kth order moment, [X unit]^k
$n(X)$ = (surface) density function of X, [X unit]$^{-1}$
N = rotation speed rpm
N_p = number of pixels, -
P = perimeter, μm
P_{CH} = convex perimeter, μm
R_1 = inner cylinder radius, m
R_2 = outer cylinder radius, m
R_g = radius of gyration, μm
s = skewness, -
S = solidity, -
Ta = Taylor number, -
x_c, y_c = centroid coordinates, μm
x_i, y_i = pixel coordinates, μm
X = any floc property, or μm or μm^2
X_i, X_{i+1} = borders of class i, [X unit]
X_{mean} = surface mean of property X, [X unit]
Y_i = (surface) fraction of the population in class i, -

Greek letters

η = Kolmogorov microscale, μm
κ = kurtosis, -
υ = kinematic viscosity, $m^2\ s^{-1}$
σ = standard deviation, [X unit]
Ω = angular velocity, s^{-1}

Literature Cited

1. Spicer PT, Pratsinis SE, Trennepohl MD, Meesters GHM. Coagulation and fragmentation: the variation of shear rate and the time lag for attainment of steady state. *Ind Eng Chem Res*. 1996;35(9):3074–3080.
2. Serra T, Casamitjana X. Effect of the shear and volume fraction on the aggregation and breakup of particles. *AIChE J*. 1998;44(8):1724–1730.
3. Biggs C, Lant P. Activated sludge flocculation: on-line determination of floc size and the effect of shear. *Water Res*. 2000;34(9):2542–2550.
4. Bouyer D, Coufort C, Liné A, Do-Quang Z. Experimental analysis of floc size distributions in a 1-L jar under different hydrodynamics and physicochemical conditions. *J Colloid Interface Sci*. 2005; 292(2):413–428.
5. Selomulya C, Bushell G, Amal R, Waite T. Aggregate properties in relation to aggregation conditions under various applied shear environments. *Int J Miner Process*. 2004;73(2–4):295–307.

6. Coufort C, Bouyer D, Liné A. Flocculation related to local hydrodynamics in a Taylor–Couette reactor and in a jar. *Chem Eng Sci*. 2005;60(8–9):2179–2192.
7. Marchisio DL, Soos M, Sefcik J, Morbidelli M. Role of turbulent shear rate distribution in aggregation and breakage processes. *AIChE J*. 2006;52(1):158–173.
8. Prat OP, Ducoste JJ. Modeling spatial distribution of floc size in turbulent processes using the quadrature method of moment and computational fluid dynamics. *Chem Eng Sci*. 2006;61(1):75–86.
9. Oles V. Shear-induced aggregation and breakup of polystyrene latex particles. *J Colloid Interface Sci*. 1992;154(2):351–358.
10. Adler P. Streamlines in and around porous particles. *J Colloid Interface Sci*. 1981;81(2):531–535.
11. Gmachowski L. Aggregate structure and hydrodynamics of aggregated systems. *Colloids Surf A*. 2005;255(1–3):105–110.
12. Bäbler MU, Sefcik J, Morbidelli M, Bałdyga J. Hydrodynamic interactions and orthokinetic collisions of porous aggregates in the Stokes regime. *Phys Fluids*. 2006;18(1):013302–013302–17.
13. Kusters KA, Wijers JG, Thoenes D. Aggregation kinetics of small particles in agitated vessels. *Chem Eng Sci*. 1997;52(1):107–121.
14. Sato D, Kobayashi M, Adachi Y. Effect of floc structure on the rate of shear coagulation. *J Colloid Interface Sci*. 2004;272(2):345–351.
15. François R. Strength of aluminium hydroxide flocs. *Water Res*. 1987;21(9):1023–1030.
16. Spicer PT, Pratsinis SE, Raper J, Amal R, Bushell G, Meesters G. Effect of shear schedule on particle size, density, and structure during flocculation in stirred tanks. *Powder Technol*. 1998;97(1):26–34.
17. Selomulya C, Amal R, Bushell G, Waite T. Evidence of shear rate dependence on restructuring and breakup of latex aggregates. *J Colloid Interface Sci*. 2001;236(1):67–77.
18. Rahmani NHG, Masliyah JH, Dabros T. Characterization of asphaltenes aggregation and fragmentation in a shear field. *AIChE J*. 2003;49(7):1645–1655.
19. Barbot E, Dussouillez P, Bottero J, Moulin P. Coagulation of bentonite suspension by polyelectrolytes or ferric chloride: floc breakage and reformation. *Chem Eng J*. 2010;156(1):83–91.
20. Li T, Zhu Z, Wang D, Yao C, Tang H. The strength and fractal dimension characteristics of alum–kaolin flocs. *Int J Miner Process*. 2007;82(1):23–29.
21. Sorensen CM. Light scattering by fractal aggregates: a review. *Aerosol Sci Technol*. 2001;35(2):648–687.
22. Yu J, Wang D, Ge X, Yan M, Yang M. Flocculation of kaolin particles by two typical polyelectrolytes: a comparative study on the kinetics and floc structures. *Colloids Surf A*. 2006;290(1–3):288–294.
23. Soos M, Moussa AS, Ehrl L, Sefcik J, Wu H, Morbidelli M. Effect of shear rate on aggregate size and morphology investigated under turbulent conditions in stirred tank. *J Colloid Interface Sci*. 2008;319(2):577–589.
24. Harshe YM, Lattuada M, Soos M. Experimental and modeling study of breakage and restructuring of open and dense colloidal aggregates. *Langmuir*. 2011;27(10):5739–5752.
25. Köylü, Faeth G, Farias T, Carvalho M. Fractal and projected structure properties of soot aggregates. *Combust Flame*. 1995;100(4):621–633.
26. Ehrl L, Soos M, Morbidelli M. Dependence of aggregate strength, structure, and light scattering properties on primary particle size under turbulent conditions in stirred tank. *Langmuir*. 2008;24(7):3070–3081.
27. Thill A, Veerapaneni S, Simon B, Wiesner M, Bottero J, Snidaro D. Determination of structure of aggregates by confocal scanning laser microscopy. *J Colloid Interface Sci*. 1998;204(2):357–362.
28. Tang S, Preece J, McFarlane C, Zhang Z. Fractal morphology and breakage of DLCA and RLCA Aggregates. *J Colloid Interface Sci*. 2000;221(1):114–123.
29. Schuetz S, Piesche M. A model of the coagulation process with solid particles and flocs in a turbulent flow. *Chem Eng Sci*. 2002;57(20):4357–4368.
30. Vahedi A, Gorczyca B. Application of fractal dimensions to study the structure of flocs formed in lime softening process. *Water Res*. 2011;45(2):545–556.
31. Chakraborti RK, Atkinson JF, Van Benschoten JE. Characterization of alum floc by image analysis. *Environ Sci Technol*. 2000;34(18):3969–3976.
32. Tolpekin VA, Duits MHG, van den Ende D, Mellema J. Aggregation and breakup of colloidal particle aggregates in shear flow, studied with video microscopy. *Langmuir*. 2004;20(7):2614–2627.
33. Rahmani NH, Dabros T, Masliyah JH. Evolution of asphaltene floc size distribution in organic solvents under shear. *Chem Eng Sci*. 2004;59(3):685–697.
34. Nan J, He W. Characteristic analysis on morphological evolution of suspended particles in water during dynamic flocculation process. *Desalination Water Treat*. 2012;41(1–3):35–44.
35. Bouyer D, Liné A, Cockx A, Do-quang Z. Experimental analysis of floc size distribution and hydrodynamics in a jar-test. *Chem Eng Res Des*. 2001;79(8):1017–1024.
36. Kilander J, Blomström S, Rasmuson A. Spatial and temporal evolution of floc size distribution in a stirred square tank investigated using PIV and image analysis. *Chem Eng Sci*. 2006;61(23):7651–7667.
37. Frappier G, Lartiges BS, Skali-Lami S. Floc cohesive force in reversible aggregation: a Couette laminar flow investigation. *Langmuir*. 2010;26(13):10475–10488.
38. Xiao F, Lam K, Li X, Zhong R, Zhang X. PIV characterisation of flocculation dynamics and floc structure in water treatment. *Colloids Surf A*. 2011;379(1–3):27–35.
39. Bubakova P, Pivokonsky M, Filip P. Effect of shear rate on aggregate size and structure in the process of aggregation and at steady state. *Powder Technol*. 2013;235:540–549.
40. Ehrl L, Soos M, Wu H, Morbidelli M. Effect of flow field heterogeneity in coagulators on aggregate size and structure. *AIChE J*. 2010;56(10):2573–2587.
41. Gorczyca B, Ganczarczyk J. Image Analysis of alum coagulated mineral suspensions. *Environ Technol*. 1996;17(12):1361–1369.
42. Mesquita DP, Dias O, Amaral AL, Ferreira EC. Monitoring of activated sludge settling ability through image analysis: validation on full-scale wastewater treatment plants. *Bioprocess Biosyst Eng*. 2009;32(3):361–367.
43. De Temmerman PJ, Van Doren E, Verleysen E, Van der Stede Y, Francisco MAD, Mast J. Quantitative characterization of agglomerates and aggregates of pyrogenic and precipitated amorphous silica nanomaterials by transmission electron microscopy. *J Nanobiotechnol*. 2012;10:24.
44. Bottinelli N, Jouquet P, Tran TD, Hallaire V. Morphological characterisation of weathered earthworm casts by 2D-image analysis. *Biol Fertil Soils*. 2012;48(7):845–849.
45. Luckham PF, Rossi S. The colloidal and rheological properties of bentonite suspensions. *Adv Colloid Interface Sci*. 1999;82(1–3):43–92.
46. Duan J, Gregory J. Coagulation by hydrolysing metal salts. *Adv Colloid Interface Sci*. 2003;100–102:475–502.
47. Otsu N. Threshold selection method from gray-level histograms. *IEEE Trans Syst Man Cybern*. 1979;SMC-9(1):62–66.

Appendix: Principal component analysis applied to floc morphological properties

PCA was performed on the floc properties. The standardized data set was arranged in a matrix M of size $N\times p$ where N is the number of measured variables and p is the number of flocs (in one set of 70 images). The correlation matrix is computed as $R=1/NM^TM$. Its eigenvalues are the principal components (PC) and the associated eigenvectors are the coordinates in the space of the original variables. The correlation coefficient of the ith PC and the jth variable is defined by Eq. A1, where V_i is the ith eigenvector. A graphical interpretation of the PC is obtained by plotting the circle of correlation, where the abscissa and ordinate of each point are the correlation coefficients between one aggregate property and, respectively, the first and the second PC

$$r(PC_i,j)=\sqrt{PC_i}V_i(j) \tag{A1}$$

The PCA was performed on several dataset obtained at different times under different shear rates and the trend was always the same. One example is illustrated on the following.

The results of the PCA performed on the floc properties area (A), perimeter (P), circle equivalent diameter (CED), major axis (L), radius of gyration (R_g), aspect ratio (AR), solidity (S), circularity (Ci), and convexity (Cv) are summarized on Figure A1.

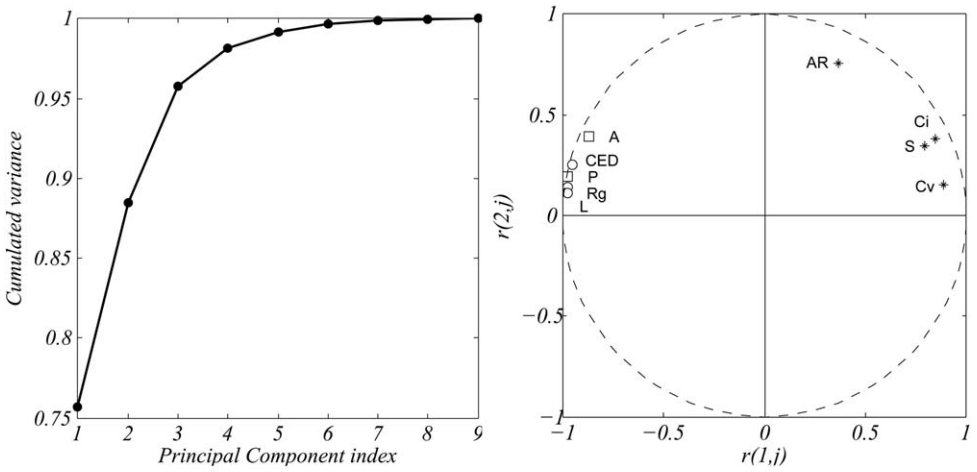

(a) Cumulated Variance (b) Circle of Correlation

Figure A1. Results of the PCA performed on nine aggregate properties.

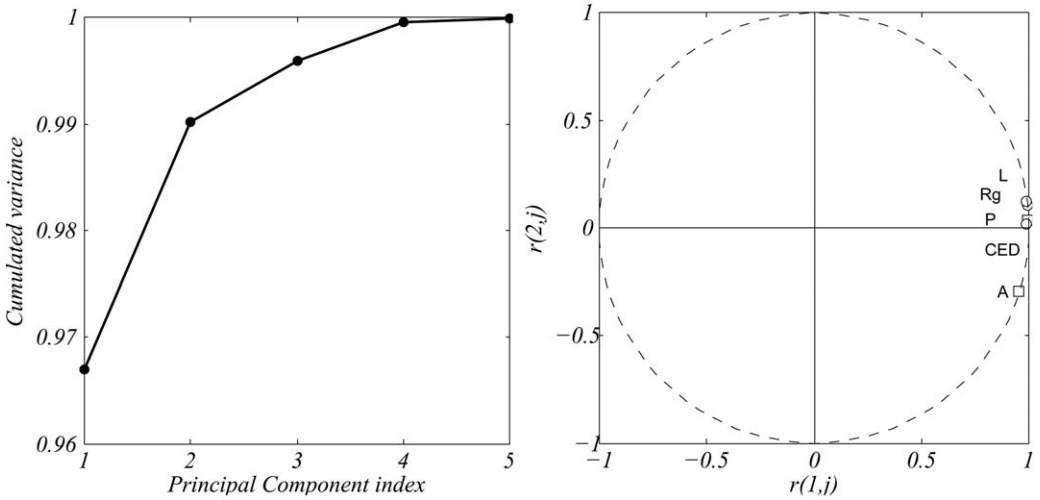

(a) Cumulated Variance (b) Circle of Correlation

Figure A2. Results of the PCA performed on size properties *A*, *P*, CED, R_g, and *L*.

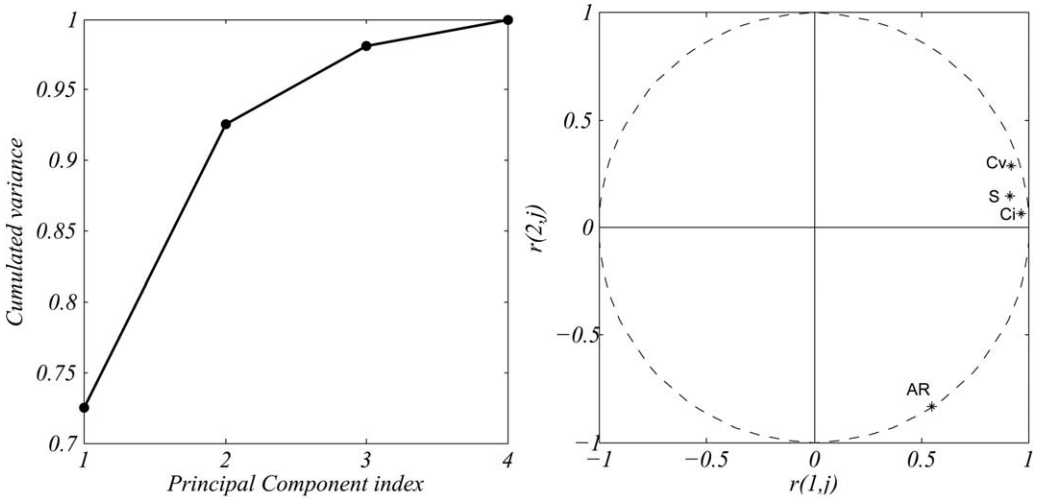

(a) Cumulated Variance (b) Circle of Correlation

Figure A3. Results of the PCA performed on shape properties AR, *S*, Ci, and Cv.

The cumulated variance plotted on Figure A1a shows that the first two PC contain 90% of the system variance. The circle of correlation for the first two PC is plotted on Figure A1b. Two groups of measured variables are clearly identified. On the one hand, the length scales CED, L and R_g gather together with the two basic measured properties P and A to from the group of size properties. In particular, the points representing the three length scales CED, L, and R_g are extremely close to the perimeter point, meaning that these measured variables are strongly correlated; conversely, are the shape properties AR, S, Ci, and Cv. The aspect ratio AR is isolated and it could be regarded as not included in the group.

To select one property from each of the two groups thus defined, PCA was performed on each one of them. Figure A2 shows the PCA results on the size properties. According to Figure A2a, the first PC represents close to 97% of the variance contained in the group of size properties. Figure A2a confirms that the length scales are strongly correlated. Depending on the dataset studied, P or R_g is the property the most correlated to the first PC. Since it is more convenient to work with a characteristic size, in the generally accepted sense, than with a perimeter, the radius of gyration is chosen as a characteristic length scale to be used in the description of the floc population (CED and L would also be appropriate because of almost equally high correlation coefficients). Among the shape group, Figure A3 shows that the first PC represents 73% of the variance. On Figure A3b, AR is isolated from S, Ci, and Cv. Ci is the property the most related to the first PC. For this reason, we propose the circularity as a relevant shape property to be studied.

Manuscript received Dec. 9, 2013, and revision received Jan. 31, 2014.